Hypervelocity impacts into porous graphite: Experiments and simulations

David Hébert, Gabriel Seisson, Jean-Luc Rullier, Isabelle Bertron, Ludovic Hallo, Jean Marc Chevalier, C. Thessieux, Francois Guillet, Michel Boustié, Laurent Berthe

Hypervelocity impacts into porous graphite: experiments and simulations

D. Hébert[1], G. Seisson[1], J.-L. Rullier[1], I. Bertron[1], L. Hallo[1], J.-M. Chevalier[1], C. Thessieux[1], F. Guillet[2], M. Boustie[3] and L. Berthe[4]

[1]CEA CESTA, 15 avenue des Sablières CS60001, 33116 Le Barp Cedex, France

[2]CEA LR, BP 16, 37260 Monts, France

[3]Insitut P' UPR3346 CNRS-ENSMA-Université de Poitiers, 1 avenue Clément Ader, 86961 Futuroscope Cedex, France

[4]Laboratoire PIMM UPR8006 CNRS-Arts et Métiers ParisTech, 151 boulevard de l'Hôpital, 75013 Paris, France

DH, 0000-0003-3926-5228

Subject Areas:
high pressure physics, materials science, computational mechanics

Keywords:
graphite, impact, cratering, steel, fragmentation, yield strength

Author for correspondence:
D. Hébert
e-mail: david.hebert@cea.fr

We present experiments and numerical simulations of hypervelocity impacts of 0.5 mm steel spheres into graphite, for velocities ranging between 1100 and 4500 m s^{-1}. Experiments have evidenced that, after a particular striking velocity, depth of penetration no longer increases but decreases. Moreover, the projectile is observed to be trapped below the crater surface. Using numerical simulations, we show how this experimental result can be related to both materials, yield strength. A Johnson–Cook model is developed for the steel projectile, based on the literature data. A simple model is proposed for the graphite yield strength, including a piecewise pressure dependence of the Drucker–Prager form, which coefficients have been chosen to reproduce the projectile penetration depth. Comparisons between experiments and simulations are presented and discussed. The damage properties of both materials are also considered, by using a threshold on the first principal stress as a tensile failure criterion. An additional compressive failure model is also used for graphite when the equivalent strain reaches a maximum value. We show that the experimental crater diameter is directly related to the graphite spall strength. Uncertainties on the target yield stress and failure strength are estimated.

This article is part of the themed issue 'Experimental testing and modelling of brittle materials at high strain rates'.

1. Introduction

The dynamic behaviour of composite materials under hypervelocity impacts (HVI) is a major concern for the aerospace industry, and a challenging problem for simulation [1–6]. The range of materials exposed to HVI continuously increases. Metals have been widely studied, both experimentally [7] and using hydrocodes [8]. Owing to their low density and high mechanical properties, composite materials are now more and more used in the aerospace industry. For instance, the behaviour of composites with carbon components has been examined under HVI [9,10]. Thus, in order to improve the predictive capabilities of hydrodynamic simulations for such materials, HVI studies on graphite are of particular interest. Published experimental results give crater dimensions in porous graphite for a large variety of projectile materials and velocities [11]. However, it has been shown that in the case of a steel sphere projectile, it remains buried below the surface of the crater [12]. For the highest velocities, i.e. above $4000\,\mathrm{m\,s^{-1}}$, hydrodynamic simulations have been used to explain this behaviour, likely related to the damage and rupture process in graphite [12]. More recent results have been obtained at lower velocities, down to $1200\,\mathrm{m\,s^{-1}}$, which show that the projectile penetration depth (PPD) follows a non-monotonic evolution, where the plasticity and rupture of the steel sphere are expected to play a major role [13]. Similar experimental results showing a decrease in penetration depth after a particular striking velocity have also been shown for spherical-nose steel projectiles striking aluminium targets by Forrestal and Piekutowki, emphasizing the effect of the projectile strength [14].

Indeed, this has been confirmed by hydrodynamic simulations [15] where a specific procedure was used to estimate the mechanical properties of the projectile and the target. This procedure allowed a first evaluation of the pressure-dependent yield stress of graphite, but owing to the simplicity of the plasticity model for the steel projectile (perfect plasticity with constant yield strength), its precision was questionable.

The purpose of this work is:

- to improve the accuracy of the simulations by using a more complex plasticity model for steel, which will help us to estimate the uncertainties on the graphite yield stress determined by our procedure and
- to propose a simple failure model for the graphite target, allowing the simulations to reproduce the experimental crater diameter and the size of damaged material.

The experiments and numerical tools are described in §2. Then, answers to the two objectives listed above are provided in §3, where simulation results are presented and compared with experiments.

2. Material and methods

(a) Experiments

Cratering experiments have been conducted with 0.5 mm diameter AISI 52100 steel spherical projectiles (hardened in the range 60–65 HRC) and 30 mm diameter, 15 mm long graphite targets. This graphite, named EDM3, is a commercial grade from the POCO company www.poco.com) and is macroscopically isotropic with a $1754\,\mathrm{kg\,m^{-3}}$ density. The main mechanical characteristics of EDM3 are summarized in table 1, and its behaviour under confined (oedometric) compression is illustrated in figure 1. More details can be found in [12,13,15,16] and at www.poco.com.

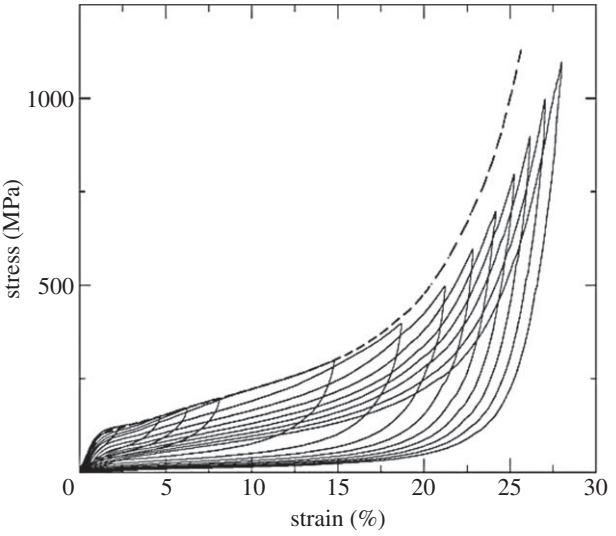

Figure 1. Experimental behaviour of EDM3 under simple (dashed line) and cycled (solid line) oedometric compression tests.

Table 1. Mechanical characteristics of EDM3.

density (kg m^{-3})	porous	1754
	compact	2265
Young modulus (GPa)	tension	11
	compression	12
failure stress (MPa)	tension	70
	compression	140
failure strain (%)	tension	1
	compression	8
bulk modulus (GPa)		9.6
Poisson ratio		0.3
porosity (%)		20

Projectiles were launched by MICA, a two-stage light-gas gun [12], at velocities ranging between 1100 and 4500 m s^{-1}. They orthogonally impacted the cylindrical graphite targets, creating a crater on the front surface. Post-test tomographies revealed that, in most cases, the projectile remains are buried into the sample (cf. figure 2*a*). Figure 2 shows the main dimensions such as diameter, depth and volume of the apparent crater and the maximum depth of the projectile. All details concerning the shot characteristics and the dimensions are given elsewhere [13]. The main data are recalled in table 2, and we just provide here a summary of the observations:

— in the first regime, called R1, and which corresponds to impact velocities below 2000 m s^{-1}, the projectile remains roughly spherical and its penetration depth linearly increases with impact velocity;
— at higher impact velocities, a second regime (R2) corresponds to plastic deformation of the projectile (with beginning of damage as shown in figure 2*c*), associated with a strong and continuous decrease of the penetration depth as impact velocity increases; and
— for impact velocities exceeding approximately 3200 m s^{-1}, projectile fragmentation is observed and its penetration depth is almost constant (regime R3).

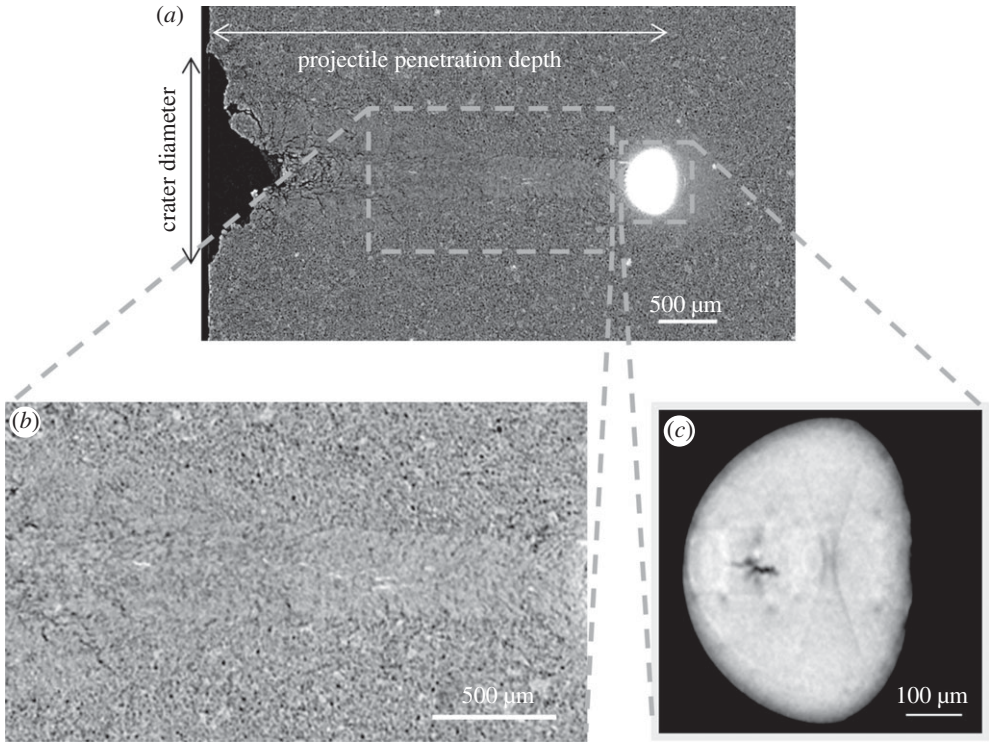

Figure 2. Slice from the post-test tomography (3.5 µm per px) of a MICA shot at 2685 m s^{-1}, corresponding to regime R2. (*a*) Black: empty spaces (crater, cracks); grey: EDM3 graphite; white: steel from projectile (coming from the left), showing strong deformation. (*b*) Magnified view of the damaged zone along the projectile path. (*c*) Magnified view of the projectile with grey rescaling, suggesting incipient cracking.

The succession of these three regimes suggests that the PPD is strongly related to the projectile dynamic behaviour, and not only to the target one. The crater diameter has also been measured. Contrary to the PPD, its evolution with impact velocity is monotonic, and no obvious distinction between different regimes could be made.

We now present the numerical tools that we have used to interpret these experimental results.

(b) Numerical tools

(i) Hydrocode

Simulations have been made with the Eulerian hydrocode Hesione developed at CEA. This code solves multi-material flow equations on a two-dimensional Cartesian grid with axial symmetry, using the BBC numerical scheme [17]. In this study, the mesh size was 12.5 µm, and we checked that the simulation results (projectile deformation, PPD, crater width, extension of damaged zone) were not sensitive to further mesh refinement. The Hesione code solves the three conservation equations (mass, momentum and energy) where stress tensor $\overline{\overline{\sigma}}$ is split into two parts: $\overline{\overline{\sigma}} = -P\overline{\overline{I}} + \overline{\overline{S}}$, where $\overline{\overline{I}}$ is the identity matrix, P is the pressure (or hydrostatic stress) and $\overline{\overline{S}}$ is the deviatoric stress tensor, such as $\mathrm{tr}(\overline{\overline{S}}) = 0$.

— The pressure P is calculated by means of an equation of state (EOS).

— The deviatoric stress tensor $\overline{\overline{S}}$ is computed by an incremental constitutive relation and limited by a Von Mises criterion: $\sqrt{(3/2)\,\overline{\overline{S}} : \overline{\overline{S}}} \leq Y$, where Y denotes the yield stress and may be a function of other local variables, such as strain, strain rate or

Table 2. Main characteristics and dimensions for shots on EDM3. Dimensionless sizes are calculated with the initial projectile diameter dp and volume vp.

shot number	proj. velocity (m s^{-1})	crater depth pc (mm)	crater diam. dmoy (mm)	crater vol. vc (mm3)	proj. depth pb (mm)	dimensionless sizes			
						pc/dp	dc/dp	pb/dp	vc/vp
02_12	1168	0.26	0.96	0.05	2.53	0.52	1.92	5.06	0.76
03_12	1695	0.40	1.28	0.15	4.02	0.8	2.56	8.04	2.29
01_12	1753	0.38	1.2	0.11	4.07	0.76	2.4	8.14	1.68
68_13	1872	0.43	1.375	0.21	4.36	0.86	2.75	8.72	3.21
70_13	2445	0.54	1.69	0.33	4.52	1.08	3.38	9.04	5.04
72_13	2685	0.74	1.86	0.59	4.22	1.48	3.72	8.44	9.01
71_13	2856	0.94	2.065	0.71	3.84	1.88	4.13	7.68	10.85
38_09	3072	1.29	3.21	3.43	0	2.58	6.42	0.00	52.41
120_12	3446	1.34	3.155	3.68	2.59	2.68	6.31	5.18	56.23
41_09	3788	0.94	2.94	2.8	0	1.88	5.88	0.00	42.78
41_01	3895	1.42	3.42	3.6	2.62	2.84	6.84	5.24	55.00
38_01	4003	1.46	3.37	3.9	2.75	2.92	6.74	5.50	59.59
39_09	4348	1.42	3.64	5.16	2.28	2.84	7.28	4.56	78.84
21_01	4512	1.85	3.945	6.3	2.31	3.7	7.89	4.62	96.26

pressure or temperature. In the principal system, the extreme deviatoric stresses are $S_{\max} = \max(S_i)_{i=1,3}$ and $S_{\min} = \min(S_i)_{i=1,3}$.

Damage can be included in the simulations. For each material, a criterion is specified. If one criterion is exceeded in a mesh, then a cavitation algorithm relaxes pressure and stresses to zero, and sets a damage variable to 1. This variable, wherever equal to 1, sets the material tensile strength to zero.

(ii) Material models

Steel

The projectile EOS is described with the 4272 SESAME table of stainless steel. A lack of knowledge persists for its constitutive relations. Indeed, the very small size of the steel spheres (500 µm) strongly limits the possibility of elementary dynamic testing. In a previous study [15], we have shown that an effective elastic limit Y_{st} around 3 GPa allows one to reproduce the transition between regimes R1 and R2. This high value is consistent with the high hardness required for bearings [18]. However, it was obtained by using the simplest plasticity model, assuming a constant yield stress (elastic perfectly plastic (EPP) model). However, it can be found in the literature that the real behaviour of this kind of steel is more complex, because it exhibits temperature, strain hardening and strain rate dependence [19]. For more accuracy in the simulations, an improved model is required that includes all these effects. In this work, we choose the Johnson–Cook (JC) model [20], recalled in the following equation:

$$Y_{\mathrm{st}} = [A + B\varepsilon^n][1 + C\log\dot{\varepsilon}^*][1 - T^{*m}], \tag{2.1}$$

with $\dot{\varepsilon}^* = \max(\dot{\varepsilon}, \dot{\varepsilon}_0)/\dot{\varepsilon}_0$ and $T^* = \min(\max(0, (T - T_0)/(T_{\mathrm{m}} - T_0)), 1)$, and where T_0 denotes room temperature, and $\dot{\varepsilon}_0 = 1\,\mathrm{s}^{-1}$ is a normalization strain rate. We have identified the JC coefficients

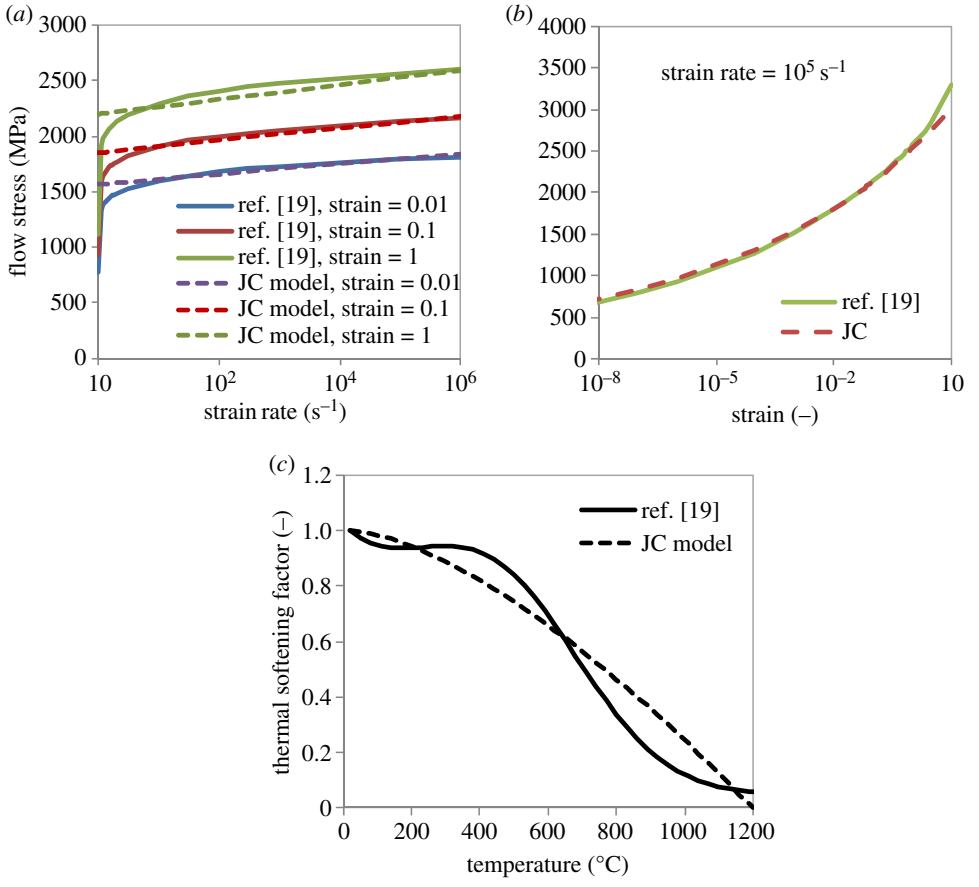

Figure 3. Comparison of our JC model with [19]. (*a*) Strain rate dependence of the flow stress for three values of plastic strain. (*b*) Strain dependence at constant strain rate of $10^5\ s^{-1}$. (*c*) Temperature dependence of the flow stress. (Online version in colour.)

Table 3. Coefficients of the JC model for steel.

A (MPa)	B (MPa)	n	C (MPa)	T_m (°C)	m	G (GPa)
200	2000	0.083	0.03	1200	1.5	80

corresponding to our steel sphere by fitting the JC model to data published in the literature [19] (assuming a hardness of 65 HRC). Note that [19] does not present experimental data for the constitutive steel of projectile with a hardness of 65 HRC, but uses various data to provide a simple model to extrapolate mechanical properties from the reference hardness to other hardnesses. Our coefficients are listed in table 3.

A comparison of our steel model with the original data from [19] is presented in figure 3. It can be seen that our JC model is satisfactory for strain rates above $10\,s^{-1}$ (figure 3*a*). We show in §3 that the strain rates in our simulations will be much above this value. As regards the strain dependence, our JC model is very close to the original data of [19] for strains that do not exceed 100% (figure 3*b*). An important feature in this JC model, when compared with the effective value of 3 GPa previously identified, is the relatively low value of 200 MPa for the initial yield stress (i.e. at small strains and small strain rates). However, we note that this feature is in accordance with [19]. The effect of this difference on the simulations is presented and discussed in the following sections. Finally, we note in figure 3*c* that the real temperature dependence is more complex than what the JC model allows: our fitting of parameters m and T_m only provides a correct average behaviour of the thermal softening factor, and the resulting parameter T_m should

not be regarded as a true melting temperature, but rather as the temperature above which strength can be neglected.

Concerning damage, [19] uses a complex criterion in which the principal and hydrostatic stress play a role. It is not implemented in Hesione, but we used it to post-process a simulation of dynamic spalling (tensile failure under uniaxial strain): the resulting spall stress was above 15 GPa, which is much above usual data [21]. The explanation is probably that this model, well adapted to simulate cutting tools, is not valid for dynamic loading. In this paper, a simpler model is used, and the rupture of the projectile is taken into account via a tensile failure criterion based on a constant spall strength Σ_{st}, i.e. failure occurs when the first principal stress exceeds this threshold. Following [15], we take $\Sigma_{\mathrm{st}} = 6\,\mathrm{GPa}$, a value that lies in the upper range of published data [21].

Graphite

The behaviour of EDM3 is described with the POREQST model [22], which supplies EOS and constitutive relations for porous materials. In the original model, the behaviour of dense material is described by a Mie–Grüneisen EOS. The following equation links the pressure P_{s} to the density ρ and the internal energy e:

$$P_{\mathrm{s}}(\rho, e) = K_{\mathrm{s}} \left(\frac{\rho}{\rho_{\mathrm{s}}} - 1 \right) \left[1 - \frac{\Gamma}{2} \left(\frac{\rho}{\rho_{\mathrm{s}}} - 1 \right) \right] + \Gamma \rho e, \tag{2.2}$$

where ρ_{s} is the density of the dense material at zero pressure and energy, K_{s} its bulk modulus and Γ is the Grüneisen coefficient. The shear modulus G_{s} and yield strength Y_{s} of the solid material are described with the following relations:

$$Y_{\mathrm{s}}(P, e) = Y_{\mathrm{g}}(P) f(e) \tag{2.3a}$$

and

$$G_{\mathrm{s}}(P, e) = G_{\mathrm{g}}(P) f(e), \tag{2.3b}$$

where f is a linear softening function decreasing from 1 to 0 when the internal energy e goes from 0 to the melting energy. Y_{g} ang G_{g} are functions of pressure, defined by linear interpolation from a set of specified values. More precisely, if $\{P_k; Y_k\}_{k=1,N}$ is the set of N values for the yield strength, with $N > 1$, the function Y_{g} is defined as follows (similar relations hold for G_{g}):

$$\left.\begin{aligned} & P < P_1 \; Y(P) \Rightarrow Y_1, \\ & P_k < P < P_{k+1} \; Y_{\mathrm{g}}(P) \Rightarrow Y_k + (P - P_k) \frac{Y_{k+1} - Y_k}{P_{k+1} - P_k} \\ \text{and} \quad & P_N < P \; Y(P) \Rightarrow Y_N. \end{aligned}\right\} \tag{2.4}$$

We note that, associated with the Von–Mises yield criterion, this piecewise linear pressure dependence can be considered as an extension of the Drucker–Prager model.

In order to take the effect of porosity into account, the POREQST model uses intermediate surfaces defined by their density ρ_i at zero pressure and energy (with $\rho_i < \rho_{\mathrm{s}}$) and also described by Mie–Grüneisen EOS

$$P_i(\rho, e, \rho_i) = K_i \left(\frac{\rho T_f}{\rho_i} - 1 \right) \quad \text{with} \begin{cases} T_f = 1 + \dfrac{\Gamma \rho_{\mathrm{s}} e}{K_{\mathrm{s}}} \\ K_i = \dfrac{K_{\mathrm{s}} f(e)}{\alpha_i + L_1(\alpha_i - 1)} \\ L_1 = \dfrac{K_{\mathrm{s}}/K_0 - \alpha_0}{\alpha_0 - 1}, \end{cases} \tag{2.5}$$

where ρ_0 and K_0 are the density and bulk modulus of the initial porous material, $\alpha_i = \rho_{\mathrm{s}}/\rho_i$ and $\alpha_0 = \rho_{\mathrm{s}}/\rho_0$. Note that this model implies that the dilatation coefficient at zero pressure is the same

```
begin
    ID←0
    If P_i(ρ,e)-S_max < σ_0(ρ,e) and P_s(ρ,e)-S_max < σ_0(ρ,e) then
        P← σ_0(ρ,e)+S_max
        ID←1                                  %% pore re-opening
    end
    If P_s(ρ,e) > P_i(ρ,e) and ID=0 then
        P← P_s(ρ,e)
        ID←3                                  %% complete densification
    end
    If P_s(ρ,e)-S_min > σ_c(ρ,e) and ID=0 then
        P← P_s(ρ,e)
        ID←3                                  %% complete densification
    end
    If P_i(ρ,e)-S_min > σ_c(ρ,e) and ID=0 then
        P← σ_c(ρ,e)+S_min
        ID←2                                  %% compaction
    end
    If P_i(ρ,e)-S_min < σ_c(ρ,e) and ID=0 then
        P← P_i(ρ,e)
        ID←0                                  %% no change of intermediate surface
    end
    If ID=1 or ID=2 then
        ρ_i ← (K_s f(e).ρ.T_f − P.ρ_s.(1+L_1)) / (K_s f(e) − P.L)   %% deduce the new intermediate surface
    end
end
```

Figure 4. Algorithm of POREQST.

whatever the intermediate surface. On these intermediate surfaces, the yield stress and the shear modulus are defined as follows:

$$Y_i(\rho, P, e, \rho_i) = \frac{Y_g(P) f(e)}{\alpha_i + L_2(\alpha_i - 1)} \quad \text{with} \quad L_2 = \frac{Y_g(P)/Y_0 - \alpha_0}{\alpha_0 - 1} \tag{2.6a}$$

and

$$G_i(\rho, P, e, \rho_i) = \frac{G_g(P) f(e)}{\alpha_i + L_3(\alpha_i - 1)} \quad \text{with} \quad L_3 = \frac{G_g(P)/G_0 - \alpha_0}{\alpha_0 - 1}, \tag{2.6b}$$

where Y_0 and G_0 are the yield stress and the shear modulus of the initial porous material.

The intermediate porous surfaces are limited in compression by the so-called compaction surface

$$\sigma_c(\rho, e) = \Sigma_c(\rho) f(e), \tag{2.7}$$

where $\Sigma_c(\rho)$ results from experimental data of a static uniaxial strain test in compression of the healthy porous material such as displayed in figure 1 (dashed line).

In traction, the limitation of the intermediate surface is undertaken by a pore re-opening curve whose intersect at zero energy with the dense material surface occurs at $(\rho_1; -P_1)$

$$\sigma_o(\rho, e) = -P_1 \frac{\rho}{\rho_1} f(e). \tag{2.8}$$

Finally, in order to establish what value of pressure the code must use, it is necessary to perform a series of tests, as shown in figure 4. The schematic in figure 5 presents a typical loading–unloading path (dashed arrow): first, the behaviour of initial porous material is described by an elastic surface; then, compaction occurs until unloading, which makes the pressure decrease elastically on an intermediate surface; if material is put under tension, it follows the same intermediate surface down to the pore re-opening surface.

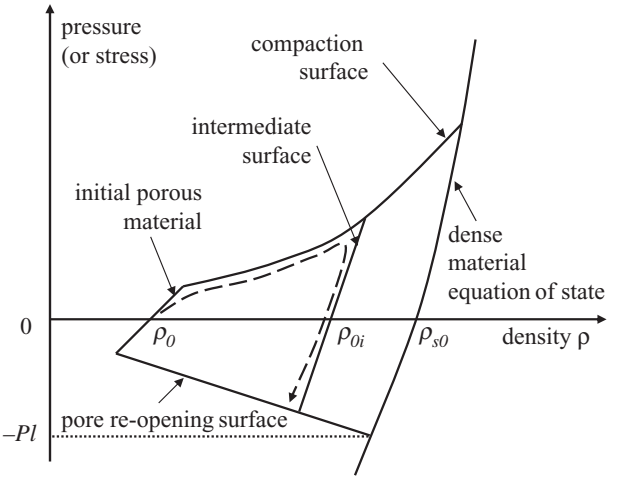

Figure 5. Schematic of the POREQST model in zero internal energy plane.

Table 4. Pressure dependence of the shear modulus of graphite.

P (GPa)	0	18	27.5
G_g (GPa)	20	50	280

Table 5. Pressure dependence of two strength models for graphite.

P (GPa)	0	25	
Yg1 (GPa)	0.1	2	
P (GPa)	0	0.5	25
Yg2 (GPa)	0.09	0.09	2

Comparison of figures 1 and 5 shows that this model is very close to the actual behaviour of EDM3 in compression. However, a difference in tension is to be noted: the POREQST model leads to permanent densification after a loading–unloading path (dashed arrow in figure 5), whereas the actual material seems to recover almost its initial density. The consequence of this on the simulation results is discussed later.

We now present the input parameters of the porous graphite model. Standard mechanical properties of EDM3 such as elastic moduli are used for K_0 and G_0. A static compression curve measured in confined tests (dashed line on figure 1) is used to model compaction. Dense graphite EOS is described with the 7832 SESAME table, which includes a description of the graphite–diamond phase transition above 20 GPa. It has been validated in laser [23] and plate impact experiments [24], where compaction is the very dominant feature. The shear modulus of dense graphite G_g is given in table 4. It has been adjusted to reproduce to sound velocity measurements under shock experiments. The simulations of these one-dimensional experiments are not sensitive to the yield stress of the material, which remains essentially unknown.

As regards constitutive relations, we chose an EPP model, but allowing a dependence with pressure. Two sets of values are used. They are referred to as Yg1 and Yg2, and the corresponding values are recalled in table 5. Yg1 has been proposed in a previous paper [15]. The second set of parameters (Yg2) corresponds to a slight reduction of Yg1, mainly at low pressures corresponding to the first part of compaction (cf. figure 1).

Concerning damage we use a simple tensile failure criterion, considering that the material breaks instantaneously when tension exceeds the so-called pore re-opening curve defined by the parameter Pl (cf. figure 5). Our model also includes an additional damage criterion based on effective plastic strain: above a specified threshold ε_g, the material loses its tensile strength, i.e. Pl is numerically set to zero in the corresponding cells. However, we do not consider here any retroaction of this criterion on the elastic–plastic compressive behaviour. Identification of parameters Pl and ε_g is presented in §3d. The study of crater diameters will lead us to use values for Pl between 200 and 140 MPa. The latter value is consistent with spall signals recorded on laser-driven shock experiments [25], and we note that it is twice as high as the static value given in table 1, which is probably owing to dynamic effects. A precise fitting of ε_g is less straightforward. No static value of this parameter being available, our choice was to allow a large variation of ε_g in order to emphasize its effect on the simulations. We thus let this parameter vary from 10% to 50%.

3. Simulation results and discussion

(a) Projectile spall strength

Results of simulations made with our steel model defined in §2b(ii) are presented in figure 6 along with experimental data. The simulations predict no damage at lower impact velocity (regime R1 and beginning of regime R2) and a complete rupture of the projectile at high impact velocities (regime R3). Between these two extreme behaviours, detailed analysis of the simulations shows that failure of the projectile occurs for impact velocities between 2900 and 3000 m s^{-1}. This threshold is slightly below the transition between R2 and R3 (approx. 3200 m s^{-1}) where the projectile fragmentation is observed in experiments, and slightly above the velocity (2685 m s^{-1}) at which incipient damage begins, as suggested in figure 2*c*.

Considering the simplicity of our failure model for the steel sphere, this agreement is satisfactory.

(b) Projectile yield strength

Below 2000 m s^{-1} (regime R1), the JC model leads to little deformation of the projectile, which remains roughly spherical (cf. figure 6). Such behaviour with EPP model required the use of a relatively high yield stress $Y_{st} = 3$ GPa [15]. As regards our JC model, for which the initial yield stress is much lower than 3 GPa, this result is due to the strain and strain rate dependence. For instance, simulations at 2000 m s^{-1} indicate that a thin (less than 40 µm) hardened layer with strains above 10%, associated with a bulk hardening owing to strain rates (more than 10^6 s^{-1}) generates sufficiently high yield stress (more than 2 GPa) to roughly preserve the spherical shape of the projectile. Thus, these simulations can be regarded as a validation of our JC model under loading conditions corresponding to regime R1.

At higher impact velocities (regime R2), simulations overestimate slightly the projectile deformation. Several reasons may explain this excessively 'soft' behaviour of our JC model. First, strain rates almost reach 10^7 s^{-1} for impact velocities of 3000 m s^{-1}, and this probably exceeds the range of validity of the data on which our JC model is fitted. Second, we know that our JC model underestimates the yield stress when plastic strains exceed 100%: this concerns a larger part of the projectile as impact velocity increases. Finally, the excessive plastic strain gives rise to high temperatures, also reducing the yield strength via the thermal softening factor.

Further improvement of the steel model may thus be possible, and we consider that our experimental data can provide useful information at higher strain rates than available, i.e. in the range from 10^5 to 10^7 s^{-1}. Indeed, the possibility of recovering the projectile inside the graphite target and the determination of its final shapes with X-ray tomography make our experiments an extrapolation of the well-known Taylor impact test [26] in the hypervelocity regime.

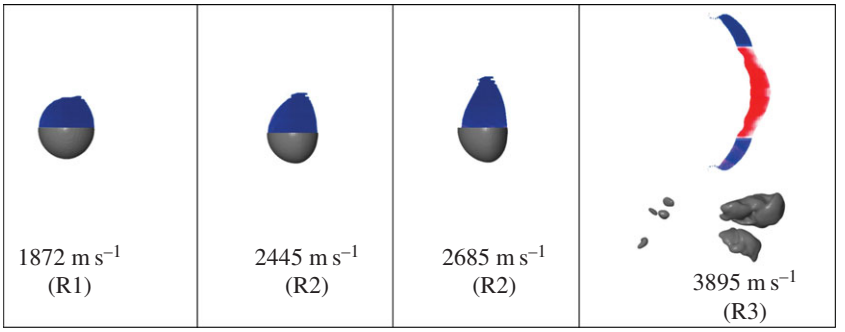

Figure 6. Final shape of the projectile (coming from the left) for four impact velocities: reconstructions from tomographies are in grey, simulation results are in a colour scale representing damage (blue for intact, red for fully damaged material). Because the projectile remains symmetric, only half of the geometry is presented for regimes R1 and R2. (Online version in colour.)

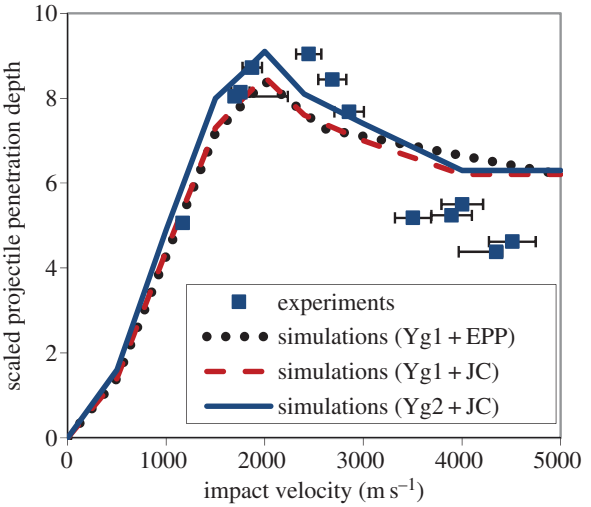

Figure 7. Comparison between the experimental results and simulations in a wide range of impact velocities. Plot of the penetration depth of the steel projectile, scaled to its original diameter. EPP and JC (respectively Yg1 and Yg2) denote the strength models of steel (resp. graphite) discussed in the text (§2b(ii)). (Online version in colour.)

(c) Graphite yield stress

The experimental and computed PPD are compared in figure 7 over a broad range of impact velocities. Two models have been used in the simulations for the steel yield strength (EPP and JC), and two models for the graphite yield strength (Yg1 and Yg2).

We first focus on the simulations with the graphite model Yg1. The JC and EPP models of steel give very similar results, and quantitative agreement with experiments is observed in regime R1. This is simply due to the fact that, as discussed in §3b, the projectile remains roughly spherical in this regime even with the JC model. The PPD is thus directly related to the graphite yield stress. Regime R2 is more complex, because plastic deformation of the projectile becomes important and also plays a role in the PPD computation. This regime is thus where the sensitivity to the steel model is expected to be the strongest. However, the JC model does not improve the simulation results in this regime, and underestimates the experimental PPD. This may be partly due to the fact that, as noted in §3b, our JC model predicts too much deformation in regime R2, causing an

excessive drag on the projectile. Another reason may come from the graphite yield strength. For this reason, a second graphite model Yg2 has also been studied.

The simulations with Yg2 show the sensitivity of the PPD to a slight reduction of the graphite yield stress. The slight increase of the simulated PPD may look like an improvement in the 1800–3000 m s^{-1} velocity range, but the PPD is then overestimated at 1100 m s^{-1}, where the steel sphere remains spherical. Thus, we cannot really discriminate between both graphite models Yg1 and Yg2. Moreover, the velocity corresponding to maximum PPD is the same with both graphite models, suggesting that the main problem remains the steel model. Finally, we use mainly Yg1 in the rest of this study.

As the main result, we observe that all simulations reproduce the non-monotonic behaviour noted in experiments. Although two-dimensional axisymmetric simulations cannot reproduce the three-dimensional aspects of projectile fragmentation observed in regime R3 (the simulations overestimate the PPD), the comparison with experimental data is satisfactory and confirms the validity of our phenomenological analysis. Finally, these results confirm the validity of the procedure that allowed the identification of Yg1 in [15].

(d) Graphite damage model

In a first step, to study the tensile failure model of graphite (parameter Pl), we have imposed the plastic threshold ε_g to 10%. Experimental results are presented in figure 8, along with simulations. The strong sensitivity of the computed crater diameter to parameter Pl is illustrated in figure 8, especially from the two simulations with the EPP model of steel, for which the best agreement with all experimental data corresponds to Pl = 200 MPa. On the contrary, the simulation with the JC model for steel would suggest to use the value Pl = 150 MPa in order to obtain similar agreement with experimental data. If we focus now on the simulations with EPP and JC using this value, then we note that the difference increases with impact velocity, and is already significant at 2000 m s^{-1}, which corresponds to the end of regime R1. This surprising result suggests that even the small deformation allowed by the JC model in regime R1 could be responsible for the difference. Thus, the confidence in the steel model seems crucial for the determination of Pl. Three arguments are in favour of the simulations with the JC model:

- this model is fitted on physical data for this kind of steel (cf. §2b(ii));
- its behaviour in regime R1 is satisfactory (cf. §3b); and
- the value Pl = 150 MPa is closer to the spall stress of 135 MPa deduced from other dynamic experiments [25].

The second notable result from figure 8 is that the simulated crater diameter shows very little sensitivity to the graphite yield stress, i.e. Yg1 or Yg2. Thus, the coupled evaluation of damage parameters Pl and ε_g will be done using Yg1.

Further simulations show that ε_g has also a notable effect. The evolution of the simulated crater diameter with impact velocity is shown in figure 9, for two values of this parameter (10% and 50%). Comparison of both simulations with Pl = 150 MPa leads to significantly different results. With $\varepsilon_g = 50\%$, it is necessary to decrease Pl from 150 to 140 MPa in order to obtain a good agreement with experimental data at high velocity. This result reveals that the sensitivity to Pl is stronger for higher values of ε_g. Finally, these two values (140 and 150 MPa) may provide upper and lower bounds of Pl.

To go further in the analysis of these results, we consider an impact at 2685 m s^{-1}, corresponding to the intermediate regime R2. The effect of ε_g on the simulated crater diameter is illustrated in figure 10, with Pl = 150 MPa. It appears that the increase of ε_g from 10% to 50% reduces the extent of the damaged zone.

Near the target surface, it also favours the propagation of a crack (owing to tensile failure) parallel to the surface. A small reduction of Pl is then sufficient to make this crack emerge on the target surface and thus contribute to the crater formation through the ejection of an annular

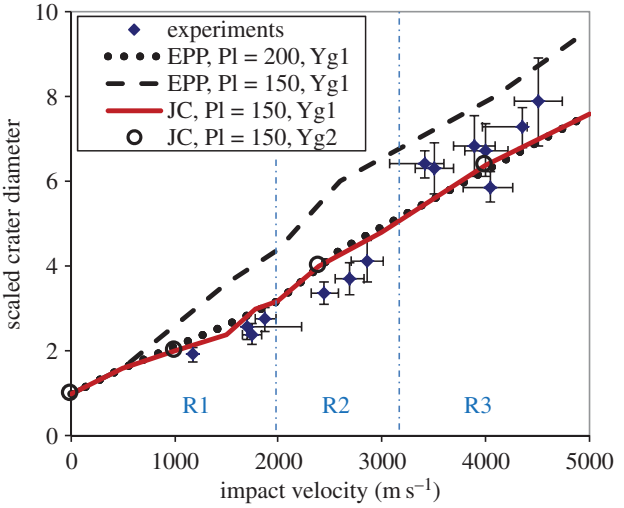

Figure 8. Comparison between the experimental results and simulations in a wide range of impact velocities. Plot of the crater diameter, scaled to the projectile original diameter. All simulations with $\varepsilon_g = 10\%$. (Online version in colour.)

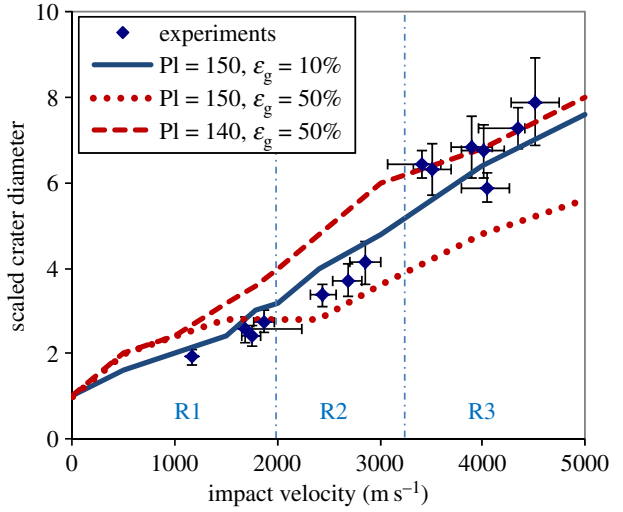

Figure 9. Plot of the crater diameter, scaled to the projectile original diameter. All simulations with Yg1. (Online version in colour.)

fragment. This annular spalling is probably a real physical mechanism, because it would be consistent with the experimental crater shape shown in figure 2*a* (corresponding to the same impact velocity). The contribution of this crack is the main mechanism that explains the increase of the simulated crater diameter in figure 9 when Pl is decreased from 150 to 140 MPa with $\varepsilon_g = 50\%$.

It appears from comparison with figure 2*b* that simulations with both values of ε_g overestimate the radial extension of the damaged zone along the projectile path. However, the simulations show strong densification of the intact material surrounding the damaged zone. The real material does not undergo such permanent densification because of the hysteresis behaviour shown in figure 1. The expected resulting movement is indicated in figure 10 with yellow arrows. Introducing this behaviour in the simulations is not possible with POREQST, but an evolution of this model has been proposed to take this into account [27]. We expect that it will help the simulations to allow more quantitative comparison with experimental observations, especially

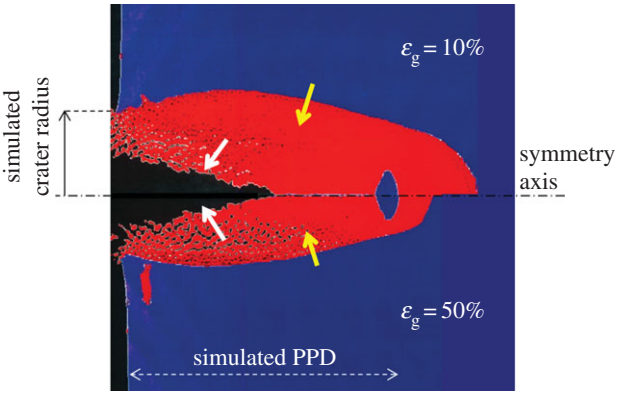

Figure 10. Impact of a steel sphere on graphite at 2685 m s^{-1}. Comparison between two axisymmetric simulations, 12 µs after impact, shows the damaged material in red and the intact material in blue. The crater filling is not achieved, and the movement of debris is indicated by white arrows. The expected movement of compressed material owing to the hysteresis behaviour is indicated by yellow arrows. (Online version in colour.)

the crater closure on the projectile path. We also observe that in the neighbourhood of the projectile, the increase of ε_g significantly reduces the extent of the damaged zone.

Finally, we note that the failure model of graphite has only minor influence on the PPD. Indeed, the main parameter acting on the PPD is the yield strength, which, in our model, is not modified by damage. Thus, the values of Pl and ε_g considered here have negligible effect on the simulations presented in §3c.

4. Conclusion

We have shown in this paper how HVIs of a steel sphere on porous graphite targets can provide useful experimental data for the modelling of both materials under dynamic loading. Post-test tomography of the recovered targets allowed a precise characterization of the projectile deformation and rupture, of its penetration depth inside the target and of the resulting crater diameter.

As regards the steel projectile, a JC model has been fitted on data from the literature. This model is found to be in good agreement with our experiments for impact velocities below 2000 m s^{-1}, because it predicts only minor deformation of the projectile. At higher impact velocities, this model slightly overestimates the projectile deformation. The high strains (approx. 1) and strain rates (10^5–10^7 s^{-1}) encountered in our experiments could be useful for further improvement of the steel model under these loading conditions. The simulations presented here have been made with a tensile failure threshold of 6 GPa, giving reasonable agreement with experiments.

As regards the graphite yield stress, the simulations presented here confirm the validity of the phenomenological analysis and of the procedure [15] that allowed the identification of this important mechanical property. With these models, our simulations reproduce the non-monotonic evolution of the PPD noted in experiments and suggest that the uncertainty associated to the determination of the graphite yield stress may not exceed 10%. Moreover, we have shown how the evolution of the experimental crater diameter with impact velocity can be used to constrain the damage model of our porous graphite with uncertainty lower than 10%. More precisely, its tensile strength has been identified to lie between 140 and 150 MPa, a value close to the spall stress deduced from other dynamic experiments [25], but almost twice the static value. Finally, the estimation of an ultimate strain in compression appears to be less straightforward. Improvement of the porous model in order to take the hysteresis into account, and further analysis of the damaged zone in the samples may help to estimate this parameter in future work.

Authors' contributions. D.H. participated in the analysis of the experimental results, ran the simulations and drafted the manuscript; G.S. participated in the analysis of the experimental results and carried out numerical developments for the simulations; J.-L.R. participated in the analysis of the results and helped draft the manuscript; I.B. carried out numerical developments for the simulations; L.H., J.-M.C. and C.T. were in charge of the experiments; F.G. carried out the tomographies; M.B. and L.B. coordinated the study. All authors gave final approval for publication

Competing interests. We declare we have no competing interests.

Funding. We received no funding for this study.

References

1. Cour-Palais B. 1999 A career in applied physics: Apollo through space station. *Int. J. Impact Eng.* **23**, 137–168. (doi:10.1016/S0734-743X(99)00069-X)
2. Davison D, Cour-Palais B, Quan X, Holmquist T, Cohen L, Ramsey R, Cummings R. 2003 Computer models of micrometeoroid impact on fused silica glass mirrors. *Int. J. Impact Eng.* **29**, 203–214. (doi:10.1016/j.ijimpeng.2003.09.017)
3. Michel Y, Chevalier JM, Durin C, Espinosa C, Malaise F, Barrau J. 2006 Hypervelocity impacts on thin brittle targets: experimental data and SPH simulations. *Int. J. Impact Eng.* **33**, 441–451. (doi:10.1016/j.ijimpeng.2006.09.081)
4. Shonberg W. 2010 Protecting earth-orbiting spacecraft against micro-meteoroid/orbital debris impact damage using composite structural systems and materials: an overview. *Adv. Space Res.* **45**, 709–720. (doi:10.1016/j.asr.2009.11.014)
5. Cherniaev A, Telichev I. 2015 Meso-scale modelling of hypervelocity impact damage in composite laminates. *Compos. Part B* **74**, 95–103. (doi:10.1016/j.compositesb.2015.01.010)
6. Yang Y, Xu F. 2015 Experimental and numerical investigation on hypervelocity impact response of 2D plain-woven C/SiC composite. *J. Mech. Sci. Technol.* **29**, 11–16 (doi:10.1007/s12206-014-1202-3)
7. Herrmann W, Jones A. 1961 Correlation of hypervelocity impact data. In *Proc. 5th Symp. on Hypervelocity Impact, Denver, CO, USA, 30 October–1 November 1961*, pp. 389–438.
8. Pierazzo E *et al.* 2008 Validation of numerical codes for impact and explosion cratering: impacts on strengthless and metal targets. *Meteoritics Planet. Sci.* **43**, 1917–1938. (doi:10.1111/j.1945-5100.2008.tb00653.x)
9. Numata D, Ohtani K, Anyoji M, Takayama K, Togami K, Sun M. 2008 HVI tests on CFRP laminates at low temperature. *Int. J. Impact Eng.* **35**, 1695–1701. (doi:10.1016/j.ijimpeng.2008.07.055)
10. Tennyson R, Lamontagne C. 2000 Hypervelocity impact damage to composites. *Compos. Part A* **31**, 785–794. (doi:10.1016/S1359-835X(00)00029-4)
11. Latunde-Dada S, Cheesman C, Day D, Harrison W, Price S. 2011 Hypervelocity impacts into graphite. *J. Phys. Conf. Ser.* **286**, 012042. (doi:10.1088/1742-6596/286/1/012042)
12. Seisson G *et al.* 2014 Dynamic cratering of graphite: experimental results and simulation. *Int. J. Impact Eng.* **63**, 18–28. (doi:10.1016/j.ijimpeng.2013.08.001)
13. Seisson G, Hébert D, Hallo L, Chevalier JM, Guillet F, Berthe L, Boustie M. 2014 Penetration and cratering experiments of graphite by 0.5-mm diameter steel spheres at various impact velocities. *Int. J. Impact Eng.* **70**, 14–20. (doi:10.1016/j.ijimpeng.2014.03.004)
14. Forrestal MJ, Piekutowski AJ. 2000 Penetration experiments with 6061-T6511 aluminum targets and spherical-nose steel projectiles at striking velocities between 0.5 and 3.0 $\mathrm{km\,s^{-1}}$. *Int. J. Impact Eng.* **24**, 57–67. (doi:10.1016/S0734-743X(99)00033-0)
15. Hébert D, Seisson G, Bertron I, Hallo L, Chevalier JM, Thessieux C, Guillet F, Boustie M, Berthe L. 2015 Simulations of hypervelocity impacts into graphite. *Proc. Eng.* **103**, 159–164. (doi:10.1016/j.proeng.2015.04.022)
16. Seisson G *et al.* 2013 Dynamic behavior of a porous brittle material: experiments and modeling. *Proc. Eng.* **58**, 715–723. (doi:10.1016/j.proeng.2013.05.083)
17. Woodward P, Collela P. 1984 The numerical simulation of two-dimensional fluid flow with strong shocks. *J. Comput. Phys.* **54**, 115–173. (doi:10.1016/0021-9991(84)90142-6)
18. Bhadeshia H. 2012 Steels for bearings. *Prog. Mater. Sci.* **57**, 268–435. (doi:10.1016/j.pmatsci.2011.06.002)

19. Umbrello D, Hua J, Shivpuri R. 2004 Hardness-based flow stress and fracture models for numerical simulation of hard machining AISI 52100 bearing steel. *Mater. Sci. Eng. A* **374**, 90–100. (doi:10.1016/j.msea.2004.01.012)
20. Johnson GR, Cook WH. 1983 A constitutive model and data for metals subjected to large strains, high rates and high temperatures. In *Proc. 7th Int. Symp. on Ballistics, The Hague, The Netherlands, 19–21 April 1983*, pp. 541–547.
21. Grady D. 1988 The spall strength of condensed matter. *J. Mech. Phys. Solids* **36**, 353–384. (doi:10.1016/0022-5096(88)90015-4)
22. Tokheim R, Curran D, Seaman L. 1973 Computational representation of constitutive relations for porous material. Technical report, no. DNA-3412F. Menlo Park, CA: Stanford Research Institute.
23. Seisson G, Hébert D, Bertron I, Videau L, Combis P, Berthe L, Boustie M. 2014 Modeling of laser-driven water-confined shocks into porous graphite. *J. Phys. Conf. Ser.* **500**, 112057. (doi:10.1088/1742-6596/500/11/112057)
24. Hébert D, Seisson G, Bertron I, Chevalier JM, Thessieux C, Quessada J, Tastet S. 2014 Plate impact experiments and simulation on porous graphite. *J. Phys. Conf. Ser.* **500**, 182016. (doi:10.1088/1742-6596/500/18/182016)
25. Seisson G *et al.* 2016 Dynamic fragmentation of graphite under laser-driven shocks: identification of four damage regimes. *Int. J. Impact Eng.* **91**, 68–79. (doi:10.1016/j.ijimpeng.2015.12.012)
26. Meyers M. 1994 *Dynamic behaviour of materials*, pp. 82–96. London, UK: John Wiley & Sons.
27. Jodar B, Seisson G, Hébert D, Bertron I, Boustie M, Berthe L. 2016 Enhancement of a dynamic porous model considering compression-release hysteresis behaviour: application to graphite. *J. Phys. D: Appl. Phys.* **49**, 325301. (idoi:10.1088/0022-3727/49/32/325301)